Triangulated Transmitter Coils With High Design Freedom for Free-Positioning and Omnidirectional Wireless Power Transfer System

Yi Li, *Student Member, IEEE*, Yuan Feng, and Yongxin Guo, *Fellow, IEEE*

***Abstract*—This article presents a novel framework for designing planar transmitter (Tx) coils to mitigate coil misalignment issues in wireless power transfer (WPT) systems. The proposed triangulated Tx coils, composed of multiple triangular unit cells, offer high design freedom in terms of size and shape. Moreover, with the proposed stitched winding technique, the current direction within each coil segment can be altered, enabling precise manipulation of the resultant magnetic field. However, this flexibility comes with the challenge of introducing new coil segments that have the potential to reduce and interfere with the magnetic field. Therefore, a robust modeling approach is developed to accurately and rapidly predict the magnetic field generated by arbitrary coil configurations in the presence of shielding structures. Then, a two-objective optimization is performed to find the optimal current directions and excitation strategy, concerning both receiving stability and intensity. The theoretical analysis and simulation results show that the proposed Tx coils can obtain 3-D rotating magnetic fields within the whole charging area, where a planar single-axis coil is sufficient to realize free-positioning omnidirectional WPT. The experimental results validate that over 94% uniformity can be achieved in terms of both angular and lateral misalignment. When using one receiver coil, a dc–dc power efficiency of 2.137% can be achieved.**

***Index Terms*—Coil design, free positioning, omnidirectional wireless power transfer (WPT), rotating magnetic field.**

I. Introduction

WIRELESS power transfer (WPT) technology has emerged as a leading solution for overcoming the limitations of traditional power supplies. In neuroscience experiments, the wireless headstages on rodents (e.g., mice and rats) are used for stimulation, recording, and transmission of neural signals [1], [2]. WPT systems not only eliminate the need for connection wires, allowing rodents to move freely, but also ensure continuous power throughout long-term deployments. However, to avoid interfering with natural behaviors, this application imposes strict size and weight limitations on wireless headstages. Moreover, the spontaneous movements of rodents often lead to misalignment between the transmitter (Tx) and receiver (Rx) coils, which leads to a significant decrease in mutual inductance, resulting in rapid efficiency degradation [3]. To overcome this challenge, designing misalignment-insensitive WPT systems is essential.

WPT systems using Tx coils to generate rotating magnetic fields have been widely studied to mitigate angular misalignment, as their magnetic field vectors change direction over time. Compared to 3-D Tx coils [4], [5], [6], planar Tx coils are more compact, scalable, and easier to integrate [7], [8], [9], [10], [11], [12], [13], [14]. When 2-D rotating magnetic fields are generated using planar Tx coils in [7], [8], [9], and [10], the Rx coils all have at least two windings along orthogonal axes, wound around a ferrite core, to capture the magnetic flux from all directions. Compared to planar loop coils, these Rx coils occupy more space and add extra weight. To enable a single planar coil as the receiving end, a 3-D rotating magnetic field is required, where the resultant magnetic field vector is scanned in 3-D space. Such magnetic field polarization ensures that even a single-axis Rx coil can capture the magnetic flux in all directions, making it suitable for situations with limited space at the receiving end. In [11], [12], and [13], two crossed bipolar coils generate magnetic field components that are orthogonal to each other while parallel to the coil plane, whereas loop coils create a magnetic field that is perpendicular to the coil plane. Under nonidentical current excitation, these coils exhibit a 3-D omnidirectional power transmitting capability. A 3-D rotating magnetic field polarization can also be achieved by the strategic placement of meander wires [14]. However, planar coil configurations in [11], [12], [13], and [14] still suffer from low design freedom, limiting further performance improvements and customization for specific applications. In addition, magnetic field polarization at the edges is often overlooked, which hinders the achievement of 3-D polarized magnetic fields of the entire charging area and thus fails to fully mitigate angular misalignment.

To solve these problems, this article proposes a novel design of planar triangulated Tx coils to further improve the design freedom and robustness of the free-positioning and

Received 10 June 2024; revised 23 August 2024; accepted 29 September 2024. Date of publication 14 October 2024; date of current version 12 December 2024. This work was supported by the Startup Grant for Professor (SGP)–City University of Hong Kong (CityU) under Grant 9380170. Recommended for publication by Associate Editor B. K. Lee. *(Corresponding authors: Yuan Feng; Yongxin Guo.)*

Yi Li is with the Department of Electrical and Computer Engineering, National University of Singapore, Singapore 117583, and also with the National University of Singapore Chongqing Research Institute, Chongqing 215123, China (e-mail: liyi@u.nus.edu).

Yuan Feng is with the Department of Electrical and Computer Engineering, University of Singapore, Singapore 117583 (e-mail: fengyuan14@tsinghua.org.cn).

Yongxin Guo is with the Department of Electrical Engineering, City University of Hong Kong, Hong Kong SAR, China (e-mail: yongxin.guo@cityu.edu.hk).

Color versions of one or more figures in this article are available at https://doi.org/10.1109/TPEL.2024.3480319.

Digital Object Identifier 10.1109/TPEL.2024.3480319

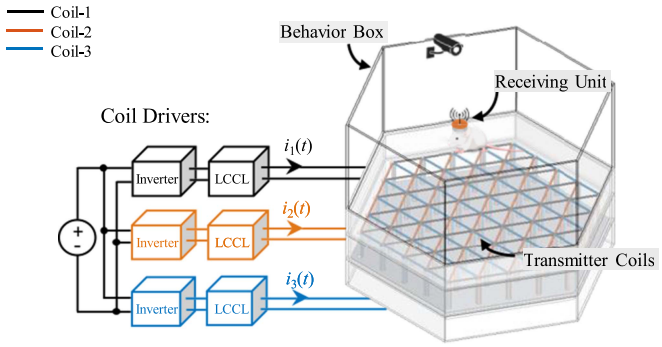

Fig. 1. Illustration of a free-positioning and omnidirectional WPT system for powering the moving receiving units within the behavior box.

omnidirectional WPT capability, which is achieved by producing three-dimensional rotating magnetic fields in the entire charging area with a highly uniform magnetic field density distribution. The main contributions of this article are listed as follows.

1) The current direction of coil segments within each unit cell can be controlled, enabling the Tx coils to achieve robust 3-D polarized magnetic fields even at the edges while providing significant flexibility in coil design.
2) An innovative winding technique is proposed, allowing the arbitrary change in the current direction of each coil segment.
3) A shielding method utilizing both magnetic and metallic materials is implemented to effectively shield the unwanted interference introduced by the proposed winding technique.
4) A precise and fast magnetic field modeling method is established to accurately predict the resultant magnetic field polarization and distribution under the proposed winding and shielding techniques.
5) The proposed WPT operates at 6.78 MHz, which lies within the Industrial, Scientific, and Medical band and complies with the Air–Fuel Alliance Standard. The megahertz operation helps to improve the charging spatial freedom under weak coupling conditions since the time-varying electromotive force (EMF) on the Rx coil is proportional to the operating frequency.
6) Genuinely free-positioning omnidirectional charging with high receiving uniformity is produced across the entire charging area.

II. Proposed Triangulated Transmitter Coils and Generated Magnetic Field

The proposed free-positioning and omnidirectional WPT system is present in Fig. 1, where three planar Tx coils and corresponding excitation circuits are placed under the behavior box, with a planar loop coil used as the receiving end. To validate the feasibility of the proposed Tx coils, the magnetic flux density $\mathbf{B}$ generated at the observation point $\mathbf{r}$ can be calculated using Biot–Savart Law

$$\mathbf{B}(\mathbf{r}) = \frac{\mu_0}{4\pi}\int \frac{Id\mathbf{L}\times\mathbf{r}'}{|\mathbf{r}'|^3} = b(\mathbf{r})I \tag{1}$$

where μ_0 is the magnetic permeability in free space, $Id\mathbf{L}$ is the wire element $d\mathbf{L}$ carrying current I, and $\mathbf{r}'$ $(=\mathbf{r}-\mathbf{L})$ is the displacement vector from wire element $d\mathbf{L}$ at $\mathbf{L}$ to the observation point $\mathbf{r}$. $b(\mathbf{r})$ is separated from $\mathbf{B}(\mathbf{r})$ to describe the influence of coil structure

$$b(\mathbf{r}) = \frac{\mu_0}{4\pi}\int \frac{d\mathbf{L}\times\mathbf{r}'}{|\mathbf{r}'|^3} = x_i\hat{x} + y_i\hat{y} + z_i\hat{z}. \tag{2}$$

Here, x_i, y_i, and z_i are the magnetic field components generated by Coil-i along x-, y-, and z- directions. In this design, amplitude-modulated (AM) currents are utilized to generate a 3-D rotating magnetic field. The excitation current of Coil-i can be defined as follows:

$$i_i(t) = I_i\cos(\omega_m t + \phi_{mi})\cos(\omega_o t + \phi_i), i = 1,2,3 \tag{3}$$

where I_i is the peak amplitude of $i_i(t)$, ω_m $(=2\pi f_m)$ and ω_o $(=2\pi f_o)$ are the modulation angular frequency and system angular frequency, respectively. ϕ_{mi} and ϕ_i are phase angles in modulation and carrier signals. Equation (3) can be further decomposed into upper sideband and lower sideband

$$i_{i|\omega_u,\omega_l}(t) = \frac{I_i}{2}\cos((\omega_o \pm \omega_m)t + (\phi_i \pm \phi_{mi})) \tag{4}$$

where ω_u $(=\omega_o+\omega_m)$ and ω_l $(=\omega_o-\omega_m)$ are corresponding upper angular frequency and lower angular frequency. Given that ω_o is significantly higher than ω_m, both the upper sideband frequency ω_u and the lower sideband frequency ω_l are approximately equal to ω_o. The total magnetic flux density $\mathbf{B}_t$ is the sum of the magnetic flux density generated by three Tx coils, which can be formulated as

$$\begin{aligned}\mathbf{B}_t &= \begin{bmatrix}B_x\\B_y\\B_z\end{bmatrix} = \begin{bmatrix}B_{x1}\\B_{y1}\\B_{z1}\end{bmatrix} + \begin{bmatrix}B_{x2}\\B_{y2}\\B_{z2}\end{bmatrix} + \begin{bmatrix}B_{x3}\\B_{y3}\\B_{z3}\end{bmatrix}\\ &= \begin{bmatrix}\mathbf{I}_1x_1 + \mathbf{I}_2x_2 + \mathbf{I}_3x_3\\ \mathbf{I}_1y_1 + \mathbf{I}_2y_2 + \mathbf{I}_3y_3\\ \mathbf{I}_1z_1 + \mathbf{I}_2z_2 + \mathbf{I}_3z_3\end{bmatrix}\end{aligned} \tag{5}$$

where $\mathbf{I}_i$ is the phasor form of current $i_i(t)$ in (3). The magnitude of (5) can be calculated as

$$\begin{aligned}|\mathbf{B}_t| &= \sqrt{\left|\sum_{i=1}^{3}\mathbf{I}_i x_i\right|^2 + \left|\sum_{i=1}^{3}\mathbf{I}_i y_i\right|^2 + \left|\sum_{i=1}^{3}\mathbf{I}_i z_i\right|^2}\\ &= \sqrt{\sum_{j\in\{x,y,z\}}\left(\sum_{i=1}^{3}\frac{I_i j_i}{2}(C_{i+}+C_{i-})\right)^2}\end{aligned} \tag{6}$$

where $C_{i+} = \cos(\phi_i + \phi_{mi})$ and $C_{i-} = \cos(\phi_i - \phi_{mi})$. The magnetic field polarization, also known as the magnetic field trajectory, describes the trace of the total magnetic flux density vector $\mathbf{B}_t$ with time, enabling a comprehensive visualization of the magnetic field properties in terms of direction and strength. Planar loop coil is used as the Rx coil here, and $\mathbf{n}$ $(1, \theta, \phi)$ is defined as the unit vector that is perpendicular to the Rx

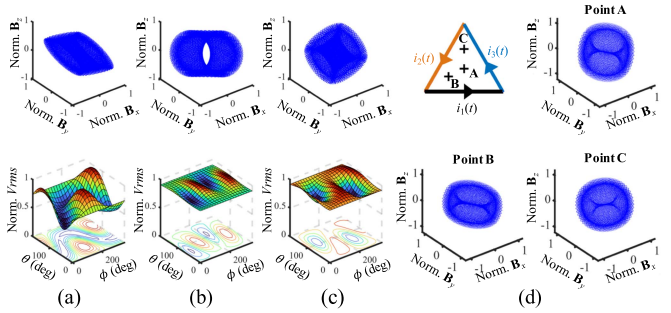

Fig. 2. Normalized polarization of magnetic flux density $\mathbf{B}_t$ and corresponding normalized induced voltage variation for different polarization types: (a) fusiform, (b) tubular, (c) spherical-like, and (d) polarization generated by three straight wires excited by currents in (3) at an observation height of 0.75 times the side length, with $I_1 = I_2 = I_3$, $\phi_{m1} = \phi_1 = \phi_3 = \pi/3$, and $\phi_{m2} = \phi_{m3} = \phi_2 = 2\pi/3$.

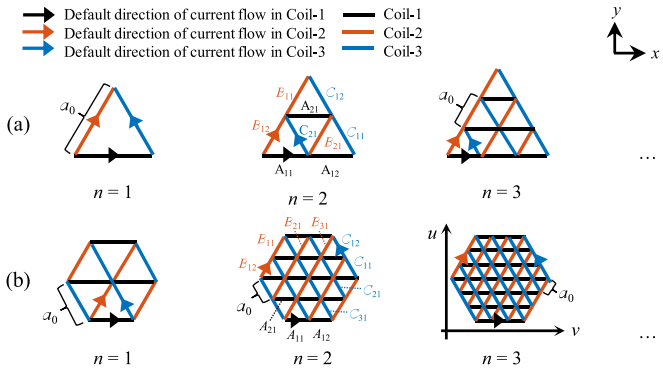

Fig. 3. Proposed Tx coils with different shapes and layers, where n represents the side length in multiples of a_0. (a) Triangular coils with n layers. (b) Hexagonal coils with n layers.

coil plane in spherical coordinate, where θ is the polar angle and ϕ is the azimuth angle. $\mathbf{n}$ is then transferred into Cartesian coordinate

$$\mathbf{n} = (n_x, n_y, n_z) = (\sin\theta\cos\phi, \sin\theta\sin\phi, \cos\theta). \quad (7)$$

The total magnetic flux Φ_B captured by the Rx coil is equal to

$$\Phi_B = \int_S \mathbf{B}_t \cdot \mathbf{n} ds = \int_S (B_x n_x + B_y n_y + B_z n_z) ds$$
$$= \sum_{i=1}^{3} i_i(t) \int_S (x_i n_x + y_i n_y + z_i n_z) ds. \quad (8)$$

Faraday's Law states that the induced voltage $\mathbf{V}_{ind}$ on the Rx coil is given by the rate of change of the total magnetic flux Φ_B

$$\mathbf{V}_{ind} = -N_r \frac{d\Phi_B}{dt} \quad (9)$$

where N_r is the number of turns of the Rx coil. The root mean square (RMS) value of induced voltage $\mathbf{V}_{\text{ind}}$ is denoted as V_{rms}. To scan all the possible orientations in a 3-D manner, the polar angle θ is changed from 0° to 180°, and the azimuth angle ϕ is changed from 0° to 360° to exhibit the receiving results of the Rx coils

$$V_{\text{rms},k} = \begin{bmatrix} V_k(\theta_1, \phi_1) & \dots & V_k(\theta_m, \phi_1) \\ \vdots & \ddots & \vdots \\ V_k(\theta_1, \phi_n) & \dots & V_k(\theta_m, \phi_n) \end{bmatrix} \quad (10)$$

where $V_{\text{rms},k}(\theta_p, \phi_q)$ (p = 1, 2, 3, ..., m, q = 1, 2, 3,..., n) is the RMS value of the induced voltage at the kth observation point when the rotation angle of the planar received coil is described by θ_p and ϕ_q. Fig. 2 exhibits how the induced voltage V_{rms} is influenced by the magnetic field polarization, using a single-turn loop coil as the Rx coil. Fig. 2(a) shows that despite achieving a fusiform 3-D rotating magnetic field, the received power remains unstable. Fig. 2(b) and (c) demonstrate that both tubular and spherical-like polarizations can greatly mitigate the angular misalignment problem. Therefore, a 3-D polarized magnetic field is essential for omnidirectional power receiving, but achieving stable receiving with planar loop coils requires careful design. In Fig. 2(d), a spherical-like rotating magnetic field polarization can be achieved using three coil segments arranged in a triangular shape. Each coil segment is excited by a different AM current. This triangular configuration can serve as a unit cell for constructing larger coils. Building on this concept, a triangulated planar Tx coil design is proposed to generate 3-D magnetic field polarization over a wide range.

As shown in Fig. 3, the proposed triangulated Tx coils are composed of multiple triangular unit cells formed by three sets of meander wires. It is assumed that the current direction can vary for each line segment. Accordingly, the direction indicators A_{direc}, B_{direc}, and C_{direc} are assigned to Coil-1, Coil-2, and Coil-3, respectively. When the direction of the actual current flow in the segment is the same as the default direction in Fig. 3, the value of the corresponding element is assigned as "+1." Conversely, the value of the direction element is assigned as '–1" when the current flow is opposite. Therefore, the elements inside the matrix are either "+1" or '–1". The direction of each line segment in the Tx coil can be written as the following matrix:

$$\Omega_{\text{direc}} = \begin{bmatrix} \Omega_{11} & \dots & \Omega_{1v} \\ \vdots & \ddots & \vdots \\ \Omega_{u1} & \dots & \Omega_{uv} \end{bmatrix} \quad (11)$$

where Ω can be A, B, and C. For A_{direc}, as shown in Fig. 3(b), the column number v increases from the left to the right along the $+x$ direction and the row number u of the line segment increases from the bottom to the top of the coils along the $+y$ direction. Therefore, the naming starting point A_{11}, which corresponds to the first row and first column of A_{direc}, is positioned at the lower-left corner of the hexagon. The naming principles of B_{direc} and C_{direc} are similar to that of A_{direc}, but the starting point changes with the coil orientation. B_{11} is obtained from A_{11} by rotating 120° clockwise around the coil center, and C_{11} is obtained from A_{11} by rotating 120° counterclockwise around the coil center.

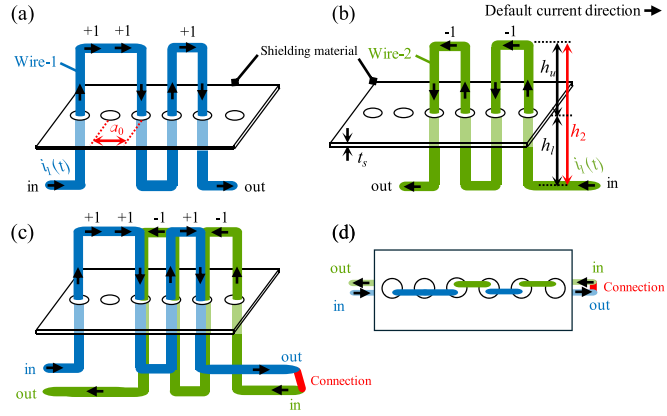

Fig. 4. Proposed stitching winding technique in the presence of shielding material. The thickness of the shielding material is denoted as t_s, and the vertical positioning of the shielding material is defined by h_u, h_l, and h_2. The designed current direction is [+1, +1, –1, +1, –1]. (a) Isometric view of Wire-1 originating from the left. (b) Isometric view of Wire-2 originating from the right. (c) Isometric view of connected Wire-1 and Wire-2. (d) Top view of connected Wire-1 and Wire-2.

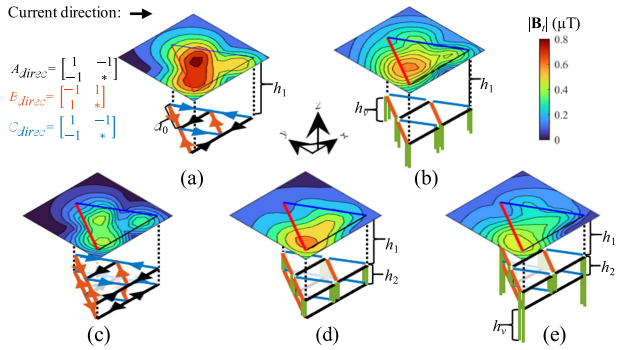

Fig. 5. Calculated magnetic flux density distribution $|\mathbf{B}_t|$ considering different coil segments of triangular coils in Fig. 3 with $n = 2$, $a_0 = 0.2$ m, and $h_1 = 0.1$ m, generated by (a) only upper coil segments, (b) upper and vertical coil segments ($h_v = 0.1$m), (c) upper and lower coil segments ($h_2 = 0.06$m), (d) upper, lower ($h_2 = 0.06$m), and vertical coil segments, (e) upper, lower ($h_2 = 0.06$m), and long vertical coil segments ($h_v = 0.4$m).

III. Proposed Stitching Winding Technique and Magnetic Shielding Modelling

It is assumed that the current direction of each line segment can be varied, which allows for the exploration of various combinations of current directions to achieve the optimal design. In the real coil design, the coil wire goes in one direction and must return to form a conduction path. To allow the current direction of each coil segment to change in the real winding, a novel winding technique is proposed in this design. Moreover, this article presents a robust modeling method to accurately and quickly predict the magnetic field of any coil configuration with a shielding structure.

A. Stitching Winding Technique (SWT)

As depicted in Fig. 4, two wires carrying identical currents initiate from opposite ends and alternately stitch through the upper and lower layers of the shielding material, termed the stitching winding technique (SWT). Fig. 4 illustrates an example of the implementation of the proposed SWT method. The current direction is set as [+1,+1,–1,+1,–1]. In Fig. 4(a), Wire-1 carrying $i_1(t)$ ascends above the shielding material for the first two segments, descends for the third, then ascends again for the fourth, and finally descends before flowing out. In Fig. 4(b), Wire-2, also carrying $i_1(t)$ but originating from the right, initially ascends, then descends in the next segment, ascends once more, and finally descends before exiting. Fig. 4(c) shows the connection between Wire-1 and Wire-2, forming a closed loop. Moreover, Fig. 4(d) presents a top view of this configuration. Compared to the ideal Tx coil configuration in Fig. 3, where the total magnetic field is simply the sum of the magnetic field generated by multiple coil segments, the real winding under SWT brings additional vertical and lower coil segments. The impact of these coil segments must be thoroughly analyzed and quantified. To visualize the influence of lower and vertical coil segments, a simple structure is studied (triangular coils with $n = 2$), and the current direction is given by

$$A_{\text{direc}} = C_{\text{direc}} = \begin{bmatrix} 1 & -1 \\ -1 & * \end{bmatrix}, B_{\text{direc}} = \begin{bmatrix} -1 & 1 \\ 1 & * \end{bmatrix}. \quad (12)$$

In the above matrix, elements without a physical meaning are indicated by an asterisk (*). Fig. 5 demonstrates the impact of different coil segments on the distribution of the total magnetic flux density $|\mathbf{B}_t|$. Fig. 5(a) shows the magnetic field distribution generated only by the upper coil segments. The presence of vertical lines results in distinct magnetic field patterns in Fig. 5(b). The difference between Fig. 5(a) and (c) demonstrates that the inclusion of lower coils with opposite current flow results in a much weaker magnetic flux density compared to the configuration where it is not included. Besides, the length of the vertical coil segment is also important as shown in Fig. 5(d) and (e). In conclusion, the magnetic field distributions in Fig. 5 generated by different combinations of upper, lower, and vertical coil segments show that each coil segment plays a critical role in shaping both the intensity and distribution of the generated magnetic field. Therefore, to accurately predict the resultant magnetic field while reducing the unwanted magnetic field, especially from the lower coil segment, a novel and robust shielding and modeling method is proposed in this article.

B. Magnetic Field Modeling (MFM) Method

It has been demonstrated that the magnetic field generated by the lower coil segments significantly reduces the overall magnetic field. Therefore, an appropriate shielding method is required to mitigate this effect. However, this poses a challenge in quickly and precisely evaluating the magnetic field generated by arbitrary windings, where the current direction of each coil segment can vary. Design based on theoretical formulas becomes highly complicated due to the nonlinear distortion of the magnetic field introduced by the shielding material. Although electromagnetic simulation with finite element method (FEM) solver can provide accurate evaluation of shielding effects, the process can be extremely time-intensive when attempting to simulate all possible configurations.

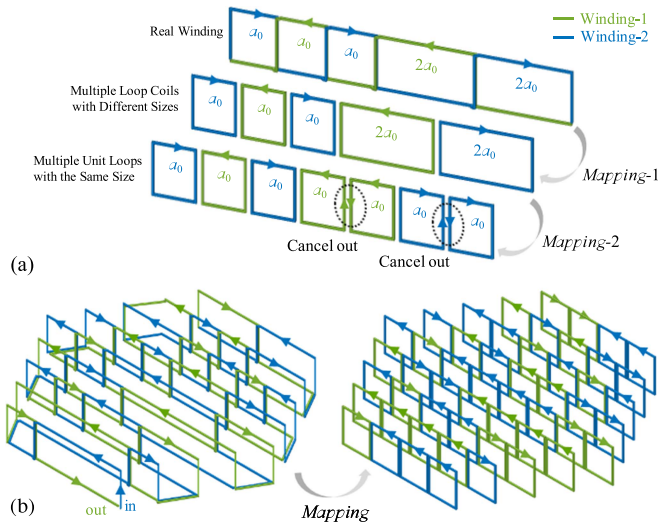

Fig. 6. Demonstration of the proposed winding equivalent method. (a) Mapping-1: Real winding to multiple loop coils with different sizes. Mapping-2: multiple loop coils with different sizes to multiple loop coils with the same size a_0. (b) Mapping example: real winding to multiple loop coils with the same size.

A novel magnetic field modeling (MFM) method is proposed in this article, aimed at achieving efficient and accurate modeling of the shielded magnetic field. Fig. 6(a) illustrates two sequential mappings. The first mapping transforms the real winding into multiple loop coils with different sizes. These equivalent loops match the exact position and direction of the currents in the original coil winding. The second mapping converts the multiple loop coils with different sizes into the multiple coils with the same sizes. Both mappings rely on the assumption that the magnetic fields generated by two adjacent straight lines with opposite currents cancel each other out. In this way, any real winding can be equivalent to a series of unit loop coils with the designated current directions. Consequently, the resultant magnetic field is the superposition of the shielded magnetic fields produced by loop coils. Fig. 6(b) shows an example that maps a real winding of Coil-1 to multiple loop coils of the same size. The shielding effect of the loop coil is then studied in the following parts.

Active and passive shielding are two dominant magnetic shielding techniques. The active shielding technique employs active coils excited by the additional source to produce magnetic fields that counteract unwanted external fields [15], while the passive shielding technique utilizes the inherent properties of the shielding material without introducing additional sources. One of the passive shielding methods involves utilizing conductive material [9], [16], where the unwanted magnetic fields are neutralized by the eddy current induced on the conductor. Another passive shielding method uses magnetic materials with high magnetic permeability, which creates a preferred path of least resistance for the magnetic field [17]. Hence, such materials can attract and guide magnetic flux, effectively redirecting it away from protected areas or confining it within the desired regions. Active shielding offers dynamic control but requires additional power and complex mechanisms, hence passive shielding is

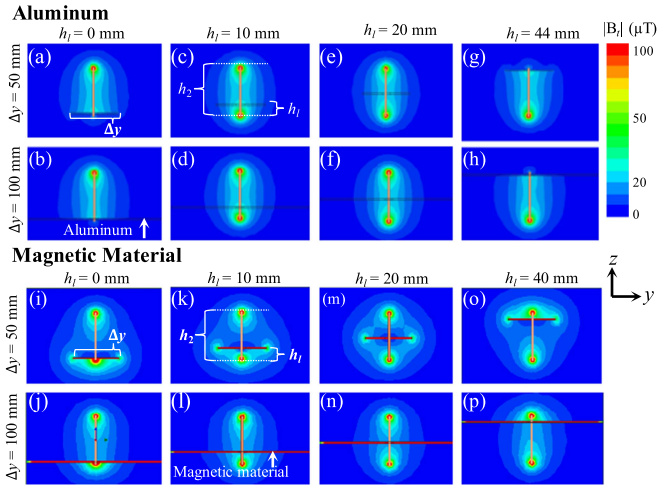

Fig. 7. Simulated magnetic flux density $|\mathbf{B}_t|$ generated by a single loop positioned along x axis, when shielded by an aluminum sheet and a magnetic material sheet, each with a thickness of 2 mm. The total height of this loop coil h_2 is fixed at 0.05 m.

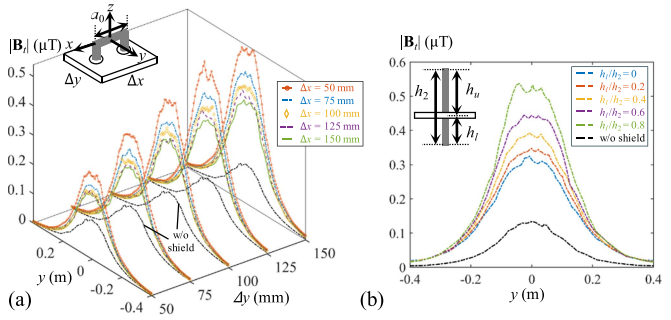

Fig. 8. Simulated magnetic flux density $|\mathbf{B}_t|$ along a line ($x = 0$, $z = 0.125$ m, $-0.4\text{ m} \le y \le 0.4$ m) generated by a loop coil and shielded by a magnetic material sheet. (a) Variations in $|\mathbf{B}_t|$ when the length Δx and width Δy of the shielding material are changing ($h_l = 0.04$ m). (b) Variations in $|\mathbf{B}_t|$ when the magnetic material sheet is positioned at different heights h_l ($\Delta x = 0.05$ m, $\Delta y = 0.15$ m).

adopted in this design. The passive shielding effects of two different materials (e.g., aluminum and magnetic material) are presented in Fig. 7. The width of the shielding structure is defined as Δy, and the vertical position of the shielding material is adjusted by varying the height h_l when the total height h_2 is fixed. As shown in Fig. 7(a), (b), (g), and (h), the magnetic fields generated by the coil segments are effectively counteracted when the aluminum plates are positioned very close to them. It is also observed that the magnetic field distribution above the upper coil segment (area of interest) does not experience obvious distortion when the aluminum sheet is positioned at the bottom or in the middle of upper and lower segments in Fig. 7(a)–(f). In addition, the shielding effect of the aluminum sheet is not sensitive to the width of the shielding material Δy in this case. When the magnetic material is positioned very close to the lower and upper coils, unlike the aluminum plate, the magnetic fields within the adjacent area are enhanced, as depicted in Fig. 7(i), (j), (o), and (p). In addition, the resultant magnetic fields vary significantly with changes in the width and position of the magnetic material, as illustrated in Fig. 7. Fig. 8(a) provides a further investigation into the complex properties when

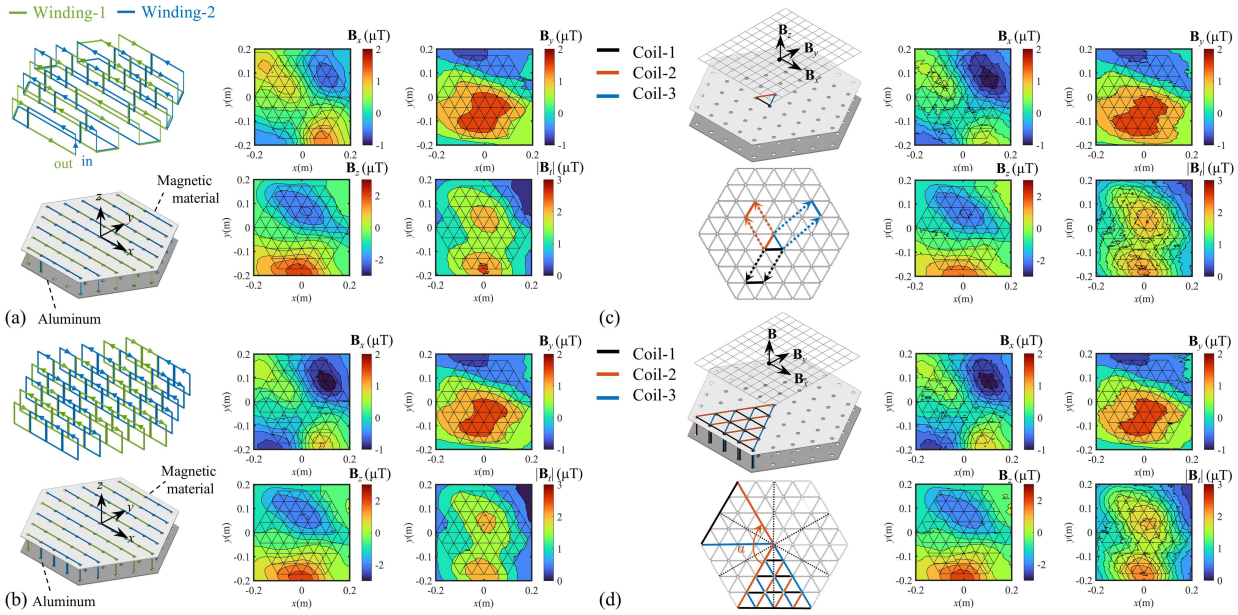

Fig. 9. Simulated distribution of x-components $\mathbf{B}_x$, y-components $\mathbf{B}_y$, z-components $\mathbf{B}_z$ of the total magnetic flux density $\mathbf{B}_t$, and total magnetic flux density $|\mathbf{B}_t|$ generated by (a) real winding, (b) multiple unit loops after equivalence. Calculated results of (c) the first approximation method, and (d) the second approximation method.

using magnetic materials, showing the variation in magnetic flux density $|\mathbf{B}_t|$ along a line directly above the loop coil. Compared to the unshielded case, the shielded $|\mathbf{B}_t|$ is substantially greater and will escalate as Δy increases and Δx decreases. Besides, an increase in the height of the shielding structure h_2 can also enhance the strength of the magnetic field $|\mathbf{B}_t|$ as demonstrated in Fig. 8(b). In conclusion, placing magnetic materials between the upper and lower coil segments can greatly enhance the magnetic flux density compared to the unshielded scenario. However, this technique is highly sensitive to the dimensions and placement of the shielding material, which complicates predictions of the resultant magnetic field. In contrast, using an aluminum sheet introduces much less magnetic field distortion but does not enhance and may even diminish magnetic field strength.

In this design, a combination of magnetic material and aluminum sheets is employed to leverage their unique properties. As shown in Fig. 9(a) and (b), a magnetic material sheet is placed proximate to the upper coil segment to strengthen the desired magnetic field, while an aluminum plate is situated just above the lower coil segment to effectively suppress undesired magnetic fields.

C. Validation of the Proposed Stitching Winding and Magnetic Field Modelling Techniques

Random current directions are used first to validate the feasibility of the proposed SWT and MFM methods. Fig. 9(a) and (b) illustrate the coil configurations for both real winding and equivalent multiple loop coils of identical size, including both shielded and unshielded versions. Fig. 9(a) and (b) also present the simulated results of x-components $\mathbf{B}_x$, y-components $\mathbf{B}_y$, z-components $\mathbf{B}_z$ of the total magnetic flux density $\mathbf{B}_t$, and the total magnetic flux density $|\mathbf{B}_t|$ generated by real winding and equivalent winding that consist of multiple unit loops, respectively. The good consistency observed between the two simulation results confirms the feasibility of the proposed SWT and MFM methods.

To further enhance the speed of magnetic field prediction and optimization, this article introduces two approximate calculation methods based on different levels of accuracy. The approximation method-1 is shown in Fig. 9(c), it is assumed that each unit loop is shielded under the same shielding structure. Initially, the magnetic field components $(\mathbf{B}_x, \mathbf{B}_y, \mathbf{B}_z)$ across the whole area of interest, generated by three different oriented unit loops, are obtained through simulation. Then, the magnetic field at other positions can be obtained by horizontal translation. The second approximation method acknowledges that the shielding effect of magnetic materials is highly sensitive to structural changes as previously discussed. As shown in Fig. 9(d), the magnetic field components $(\mathbf{B}_x, \mathbf{B}_y, \mathbf{B}_z)$ generated by 30 differently oriented and positioned unit loops are simulated. Given the central symmetry of the proposed structure, the magnetic field at other positions can be obtained by rotation.

Both calculation methods derive the magnetic field components $(\mathbf{B}_x, \mathbf{B}_y, \mathbf{B}_z)$ from FEM simulations, where the magnetic field generated by a unit loop coil is modeled in the presence of the entire shielding structure. The total magnetic field is then obtained through different methods of superposition. The main difference between these two methods lies in whether they take into consideration the variation in the shielding effects as the unit loop coil is positioned at different locations within the shielding structure.

D. Transmitter Coils Optimization

In this article, a two-objective optimization is performed to determine the optimal coil structure, direction matrix, and

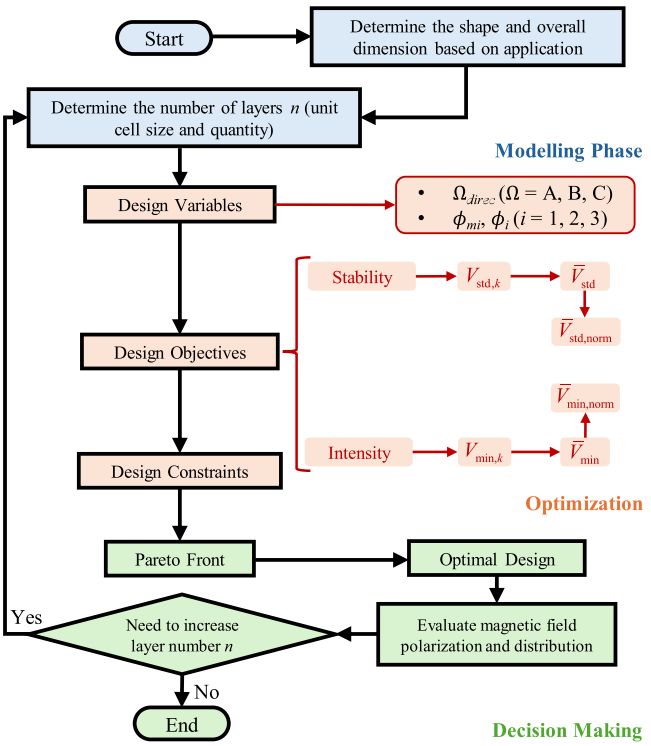

Fig. 10. Design flowchart of the two-objective optimization process.

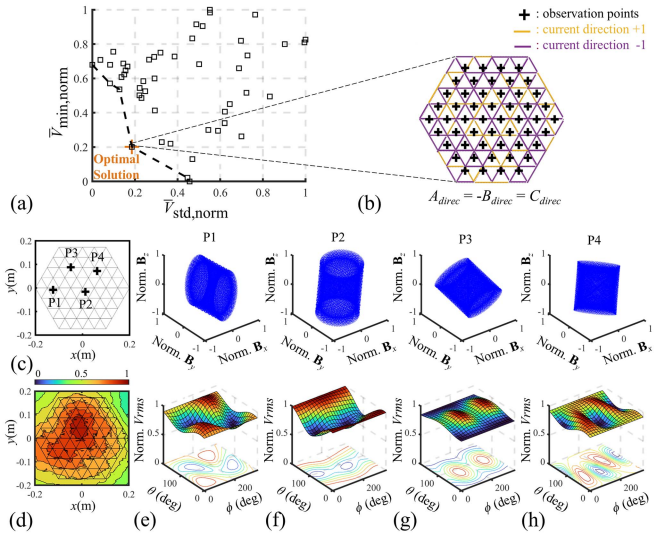

Fig. 11. (a) Derived Pareto-front resulting from the two-objective optimization. (b) Current directions A_{direc}, B_{direc}, and C_{direc} obtained from the optimal solution. (c) Observation Points: P1, P2, P3, and P4. (d) Distribution of total magnetic flux density $|\mathbf{B}_t|$. Polarization and corresponding normalized RMS value of induced voltage V_{rms} at observation points (e) P1, (f) P2, (g) P3, (h) P4.

corresponding phase angles. The detailed optimization flowchart is illustrated in Fig. 10. Initially, the shape and overall dimension of the transmitter coils are established based on the intended application with the number of layers n fixed at a predetermined value. Then, the current directions (Ω_{direc}) and the phase angles (ϕ_i, ϕ_{mi}) serve as two design variables in the optimization. Since the three Tx coils share the same structure and are symmetrically positioned about the center, the amplitudes of the three excitation currents are preset to be equal. In the optimization process, various combinations of phase angles (ϕ_i, ϕ_{mi}) are attempted, with each angle randomly selected from a phase pool. The RMS value of induced voltage V_{rms} on the Rx coil is directly related to the received power and receiving uniformity. To ensure both stable and sufficient received power at the secondary side, two optimization objectives regarding induced voltage are defined as follows.

1) *Stability:* $V_{\text{std},k}$ represents the standard deviation of the induced voltage $(V_k(\theta_1, \phi_1), \ldots, V_k(\theta_m, \phi_n))$ in (10) at the kth observation point, which is calculated as

$$V_{\text{std},k} = \sqrt{\frac{1}{N-1}\sum_{i=1}^{N} |V_{\text{rms},k} - \overline{V}_{\text{rms},k}|^2}, N = mn \tag{13}$$

where $\overline{V}_{\text{rms},k}$ is the average value of the induced voltage at the kth observation point. To minimize the fluctuation caused by the rotation, the average value of $V_{\text{std},k}$ (denoted as $\overline{V}_{\text{std}}$) across all observation points should be as small as possible. $\overline{V}_{\text{std}}$ is further normalized to $\overline{V}_{\text{std,norm}}$ using min-max normalization method [18].

2) *Intensity:* $V_{\text{min},k}$ represents the minimum induced voltage value at the kth observation point. The average value of $V_{\text{min},k}$ over all observation points is denoted as $\overline{V}_{\text{min}}$. To ensure that both optimization objectives attain their optimal values at the minimum, $-\overline{V}_{\text{min}}$ instead of $\overline{V}_{\text{min}}$, is normalized to $\overline{V}_{\text{min,norm}}$ using min-max normalization method.

The optimization problem can be summarized as follows:

$$\begin{aligned}&\text{Design Objective: Minimize } \overline{V}_{\text{std,norm}} \text{ and } \overline{V}_{\text{min,norm}}\\ &\text{Design Variables: } \Omega_{\text{direc}}(\Omega = A, B, C), \phi_{mi}, \phi_i (i = 1, 2, 3).\end{aligned} \tag{14}$$

The derived magnetic field polarization and distribution of the optimal design are checked to determine, whether the previous fixed layer number n is sufficient to meet the desired performance criteria. If the criteria are not met, increasing the number of layers n, and the optimization process is repeated. Fig. 11(a) displays the derived Pareto-optimal front after the two-objective optimization. The chosen optimal point is the one with the smallest Chebyshev distance from the ideal point (0, 0). In Fig. 11(b), the optimal result of current directions is presented. A hexagonal transmitter coil with four layers ($n = 4$) is implemented.

The corresponding phase angles are listed in Table I. This optimal combination of phase angles, 0, $\pi/3$, and $2\pi/3$, not only achieves optimal magnetic field polarization and distribution, but also minimizes the reactive power in the system caused

TABLE I
KEY PARAMETERS IN THE SYSTEM

Symbol	Value	Symbol	Value
L_i	14.13 μH	C_i, C_{ri}	39, 2500 pF
C_{bi}, C_s	330 μF 403 pF	L_{ri}, L_{bi}, L_s	0.22, 68, 1.29 μH
f_m, f_o, V_{dc}	500 Hz, 6.78 MHz, 6 V	a_0, h_1	0.05 m, 0.1 m
ϕ_1, ϕ_2, ϕ_3	$\pi/3$, $2\pi/3$, 0	ϕ_{m1}, ϕ_{m2}, ϕ_{m3}	$\pi/3$, $2\pi/3$, 0

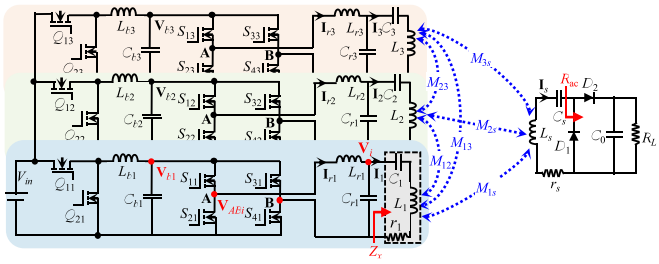

Fig. 12. Circuit topology of the proposed 3Tx-1Rx WPT system.

by the inherent mutual inductance between three Tx coils. Fig. 11(c)–(h) displays the distribution of the total magnetic flux density $|\mathbf{B}_t|$ across the entire hexagonal charging area, along with polarization at four arbitrarily selected points, and corresponding induced voltage variations.

IV. System Topology and the Proposed Excitation Strategy

Based on previous analysis, Tx coils need to be excited by AM currents with designed phase angles and amplitude. To achieve this, the circuit topology of the proposed excitation strategy is illustrated in Fig. 12. Each transmitting circuit consists of a synchronous buck converter, a full-bridge inverter, and an LCCL compensation network. First, the synchronous buck converter modulates the amplitude of its output voltage according to the envelope of the required AM currents. This is achieved by controlling the on-off states of Q_{1i} and Q_{2i}, and the output voltage $\mathbf{V}_{bi}$ is proportional to the conduction duty cycle D_{1i} of high-side switch Q_{1i}

$$V_{bi} = D_{1i}V_{in}, i = 1, 2, 3. \tag{15}$$

Then, the full-bridge inverter converts the envelope $\mathbf{V}_{bi}$ into high-frequency AM voltages $\mathbf{V}_{ABi}$ between Point-A and Point-B as shown in Fig. 12. Following this, an LCCL compensation network is used to provide controllable current sources to the Tx coils. L_{bi} and C_{bi} are inductance and capacitance in the buck converters. L_{ri}, C_{ri}, and C_i are inductance and capacitance in the LCCL-S topology. L_i and r_i represent the self-inductance and parasitic resistance of Coil-i, respectively. On the secondary side, capacitor C_s fully compensates L_s, and a voltage doubler rectifier is used to supply dc voltage to the load R_L. The mutual inductance between Tx Coil-i and Tx Coil-j is defined as M_{ij} $(i \neq j)$, and the mutual inductance between Tx Coil-i and Rx coil is defined as M_{is}. Given that the three Tx coils have an identical structure and are symmetrical about the center, the mutual inductance $M_{12} = M_{13} = M_{23} = M_0$. Since the three Tx coils are identical, the parameters of each transmitting circuit are considered to be the same for simplification, i.e., $L_{ri} = L_r$, $C_{ri} = C_r$, $L_i = L_0$, $C_i = C_0$. In Fig. 12, $\mathbf{Z}_x$ represents the overall equivalent impedance looking into the L_iC_i branch. This includes the $\mathbf{Z}_{\text{ref}}$, which is the sum of the reflected impedance from other transmitting circuits and receiving circuits. Based on Kirchhoff's voltage law, the following can be obtained:

$$\mathbf{V}_i = j\omega L_r \mathbf{I}_{ri} + Z_x \mathbf{I}_i \tag{16}$$

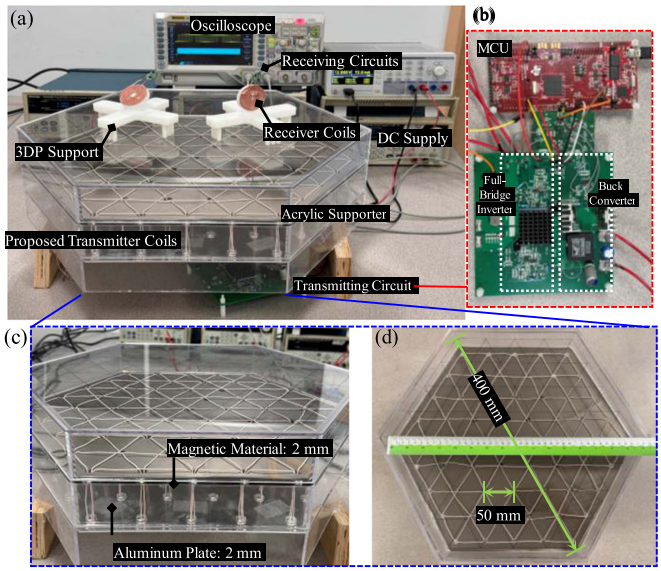

Fig. 13. Experimental verification of the proposed free-positioning and omnidirectional WPT system. (a) System set-up. (b) MCU and one of the transmitting circuits. (c) Front view of the proposed Tx coils and shielding materials. (d) Top view of the proposed Tx coils.

$$\mathbf{I}_{ri} = (j\omega C_r Z_x + 1)\mathbf{I}_i. \tag{17}$$

When the values of components in the LCCL compensation network satisfy $\omega_o = 1/\sqrt{L_rC_r}$,(16) can be rewritten as

$$\begin{aligned}\mathbf{V}_i &= j\omega L_r(1 + j\omega C_r \mathbf{Z}_x)\mathbf{I}_i + \mathbf{Z}_x\mathbf{I}_i \\ &= j\omega L_r \mathbf{I}_i - \omega^2 L_r C_r \mathbf{Z}_x \mathbf{I}_i + \mathbf{Z}_x \mathbf{I}_i = j\omega L_r \mathbf{I}_i.\end{aligned} \tag{18}$$

As a result, the output current $\mathbf{I}_i$ through Coil-i will only be determined by the voltage $\mathbf{V}_i$ and inductance L_r

$$\mathbf{I}_i = \mathbf{V}_i/(j\omega L_r). \tag{19}$$

Therefore, by utilizing the proposed excitation strategy, precise control over both the amplitude and phase angle of each excitation current can be achieved regardless of variations in load and coupling conditions.

V. Experimental Validation

A. Experimental System Set-Up

To validate the free-positioning and omnidirectional capability of the proposed triangulated coils, the complete system setup is presented in Fig. 13. This setup includes a microcontroller (MCU) TMS320F28379D, transmitting circuits, Tx coils, shielding materials, an acrylic box, 3-D printed (3DP) supports, receiving circuits, and Rx coils.

A total of six PWMxA/B modules in the MCU are used to generate control signals for on-off switches in transmitting circuits. At the front buck stage, sinusoidal pulse width modulation control signals are fed into the LMG1210 half-bridge drivers to generate control signals for Q_{1i} and Q_{2i}. For full-bridge inverters, the MCU generates a pair of inverse control signals operating at 6.78 MHz through PWMxA/B, which was then input to the LMG1210 drivers to produce control signals for the left half-bridge (S_{1i}, S_{2i}) and the right half-bridge (S_{3i},

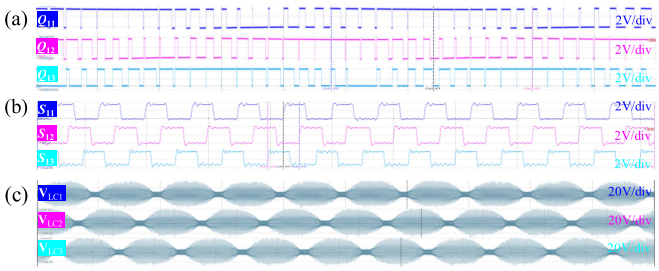

Fig. 14. Experimental waveforms: (a) Drive signals for switches Q_{11}, Q_{12}, Q_{13}. (b) Drive signals for switches S_{11}, S_{12}, S_{13}. (c) Voltage $\mathbf{V}_{LCi}$ over the combination of L_i and C_i.

S_{4i}). Dead time can be manually controlled by adjusting the external resistor connected to the LMG1210, and the phase difference between the excitation signals of the coils is managed by a synchronization program. IRLB4030PbF is utilized as the ON–OFF switch in the synchronous buck converter stage, and the GaN-on-silicon power transistor GS66508B is used in full-bridge inverters. To mitigate the skin effect at high frequencies, a litz wire comprising 500 strands of AWG 48 wires is utilized to fabricate both Tx and Rx coils. The acrylic box is a regular hexagon with a side length of 400 mm. The relative permeability of magnetic material A4000-150 exhibits a permeability value of around 135 at 6.78 MHz. The magnetic sheet, with a total thickness of 2 mm, is composed of four layers of a 0.5-mm magnetic sheet. The aluminum plate also has a total thickness of 2 mm. Moreover, circular vias are created in both the aluminum and magnetic sheets to meet precise stitching winding requirements. Essential waveforms are presented in Fig. 14, and all the key parameters in the system are listed in Table I.

B. 3-D Omnidirectional Wireless Charging

To verify the robustness of the proposed omnidirectional WPT system, a 35×35 mm circular loop coil is used as the Rx coil. The normal vector of the Rx coil plane is described by polar angle θ and azimuthal angle ϕ in the spherical coordinate system. To achieve comprehensive coverage of all possible directions in 3-D space, θ is scanned from 0° to 90°, and ϕ is scanned from 0° to 315°. During the experiment, the Rx coil is mounted on adjustable 3DP supports to achieve the specified orientations, ensuring a constant distance of 100 mm between the centers of the Tx and Rx coils. Fig. 15 illustrates the variation in RMS value of induced voltage $V_{\rm rms}$, as described in (10), at four arbitrarily selected observation points when the Rx coil is angularly misaligned. Both experimental and theoretical results are presented, and despite some errors between them, their overall trends are mostly consistent. Receiving uniformity, in terms of angular and lateral misalignment, can be quantified according to the definitions provided in [13]. The uniformity related to rotation angles at each observation point is defined as

$$U_a = N_a/N_{ta} \tag{20}$$

where N_{ta} represents the total number of selected rotation angles at each observation point, and N_a denotes the number of rotation angles where the voltage exceeds 75% of the maximum voltage.

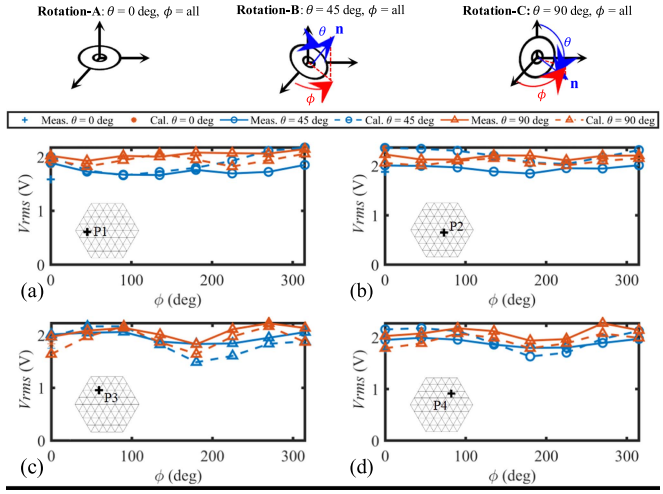

Fig. 15. Measured $V_{\rm rms}$ under different rotation types at different observation points (a) P1, (b) P2, (c) P3, and (d) P4.

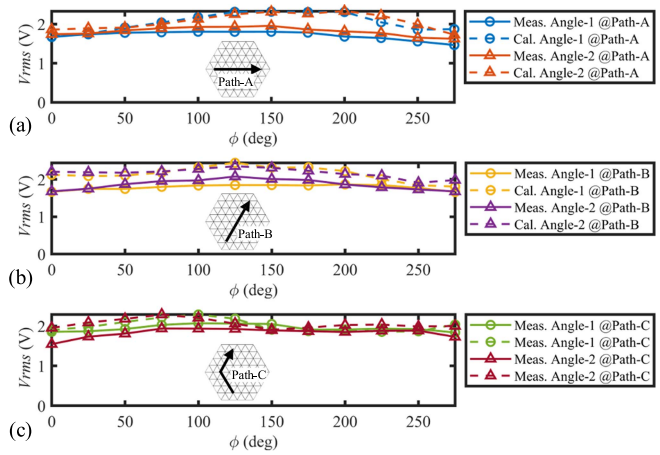

Fig. 16. Variations of measured $V_{\rm rms}$ under two orientations (Angle-1: $\theta = 0°$, Angle-2: $\theta = 45°$, $\phi = 0$) when the Rx coil moves along different paths (a) Path-A, (b) Path-B, and (c) Path-C.

At a height of 100 mm, the uniformity U_a at each selected point exceeds 94%. Therefore, the feasibility of the proposed omnidirectional powering characteristics is verified.

C. Free-Positioning Wireless Charging

Fig. 16 illustrates the variations in measured $V_{\rm rms}$ as the Rx coil moves along three different paths: Path-A, Path-B, and Path-C. Both Path-A and Path-B involve the Rx coil starting at one vertex of the hexagon and traveling to the directly opposite vertex. In contrast, Path-C follows a zigzagging route designed to cover the remaining points within the charging area. During the testing, the Rx coil moves along these paths under two different orientations. Angle-1 corresponds to the orientation where the plane of the Rx coil is parallel to the Tx coil plane ($\theta = 0°$), while Angle-2 represents the orientation where $\theta = 0°$ and $\phi = 45°$.

The measured results in Fig. 16 show that the RMS value of induced voltage $V_{\rm rms}$, as described in (10), remains fairly stable even in extreme cases, such as the start and end points of each

TABLE II
WORK COMPARISON OF FREE-POSITIONING AND OMNIDIRECTIONAL WPT SYSTEM WITH ROTATING MAGNETIC FIELDS

Paper	Tx/Rx coils dimension	Frequency	Tx size: Rx size: Separation	Omnidirectional charging with loop coils	Free-positioning charging	Design freedom	Efficiency @Rx number
[7]	2-D/2-D	280 kHz	5:1:1	No	Yes	No	33.6%@5-Rx
[9]	2-D/2-D	280 kHz	10:1:2	No	Yes	No	32%@9-Rx
[8]	2-D/2-D	280 kHz	10:1:7	No	Yes	No	8.2%@9-Rx
[14]	2-D/2-D	100 kHz	10:2:1	Yes	Yes	No	55.6%@5-Rx
[10]	2-D/2-D	6.78 MHz	100:1:0	No	Yes	No	9.3%@200-Rx
[13]	2-D/2-D	6.78 MHz	10:1:2.5	Yes	Yes	No	8.39%@5-Rx
This work	2-D/2-D	6.78 MHz	40:3.5:10	Yes	Yes	Yes	2.137%@1-Rx

path. Furthermore, the measured voltage V_{rms} is relatively weak at the edges of the Tx coils and moderately higher at the center, consistent with previous theoretical findings in Fig. 11(d). To quantitatively express the voltage fluctuation under each case, the fluctuation concerning lateral misalignment is defined as

$$U_l = N_l/N_{tl} \tag{21}$$

where N_{tl} is the number of the total selected points along each path, and N_l denotes the number of points where the voltages exceed 75% of the maximum voltage of each observation point. The results indicate that the horizontal movement of the Rx coil does not experience much degradation in all cases. The uniformity U_l reaches 100% along all three paths under both orientations. Therefore, the proposed WPT system demonstrates robust free-positioning capability throughout the entire charging area.

VI. DISCUSSION

Table II provides a comprehensive comparison of coil dimensions, operating frequency, size ratio, and other key parameters with those of other free-positioning and omnidirectional WPT systems utilizing rotating magnetic fields. In this work, the size ratio of Tx and Rx coils is deliberately made large to ensure sufficient activity space for small animals, enable independent charging, and maintain high compactness of the headstages. However, considering the significant size difference and large separation between Tx and Rx coils, the inductive link operates under low coupling conditions, which inherently results in relatively low efficiency. To address this, the operating frequency of the proposed WPT system is selected as 6.78 MHz, a frequency more suitable for WPT systems under low couplings, as the EMF on the Rx coil is proportional to the operating frequency. However, the complexities of converter design, control circuits, and wire selection escalate when the frequency climbs up to megahertz frequencies.

To further optimize the proposed design, it is essential to identify and analyze the losses within the proposed WPT system. The total loss in this system includes losses in the transmitting circuits, coil losses, losses due to the shielding material (P_{shield}), and losses in the rectifier (P_{rec}). The loss in the transmitting circuits can be further decomposed into losses in the buck stage (P_{buck}) and the full-bridge inverter (P_{inv}) [18]. Fig. 17 illustrates the loss breakdown of the proposed WPT system, where the coil loss of the three Tx coils (P_{Tx}) dominates the loss of the system, despite AWG 48 Litz wire being employed in the design. If this system is applied to scenarios where the size of the receiving end is not strictly constrained, such as charging smartphones or tablets, the operating frequency can be adjusted to a few hundred kilohertz, whereas Litz wire is more efficient at mitigating the skin effect and proximity effect. Moreover, this design can be extended to include four or more excitations, however, integrating additional circuits and coils operating at MHz frequencies may lead to increased system losses as previously discussed. Therefore, further discussion is necessary when adding coils and excitations. On the bright side, the proposed SWT and MFM methodologies in this study can be directly applied, and they have been proven effective and viable, providing a robust theoretical basis for further study. Also, considering the significant size difference between Tx and Rx coils, the system efficiency is inevitably low when there is only one Rx coil, but the efficiency will escalate with the number of receiving ends since the excitation currents through each coil are considered constant with the help of the LCCL topology.

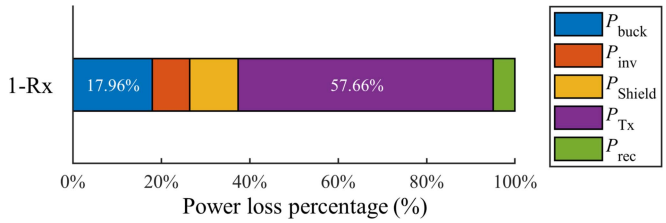

Fig. 17. Power loss breakdown of the proposed WPT system.

VII. CONCLUSION

This article introduces a novel triangulated Tx coil design, composed of multiple triangular unit cells. The design offers high degrees of design freedom, allowing customization of unit size, number of layers, and shape to meet specific requirements. Furthermore, it can adjust the current direction of each coil segment. To achieve this, an innovative winding technique is presented, enabling arbitrary change in the current direction of each coil segment. In addition, a new shielding method combining magnetic and metallic materials is proposed to effectively enhance the magnetic field strength. A precise and rapid magnetic modeling method is also developed and validated to accurately predict magnetic field polarization and distribution when using the proposed winding and shielding techniques. With the proposed excitation strategy, the planar Tx coils can generate a 3-D rotating magnetic field over a wide area, facilitating free-positioning and omnidirectional wireless power transfer using only planar loop coils. Experimental results demonstrate

that over 94% uniformity can be achieved in terms of both angular and lateral misalignment. When using one receiver coil, a dc–dc power efficiency of 2.137% can be achieved.

REFERENCES

[1] S. A. Mirbozorgi, Y. Jia, P. Zhang, and M. Ghovanloo, "Toward a high-throughput wireless smart arena for behavioral experiments on small animals," *IEEE Trans. Biomed. Eng.*, vol. 67, no. 8, pp. 2359–2369, Aug. 2020.

[2] J. P.-W. Chow, H. S.-H. Chung, L. L.-H. Chan, R. Shen, and S. C. Tang, "Optimal design and experimental assessment of a wireless power transfer system for home-cage monitoring," *IEEE Trans. Power Electron.*, vol. 34, no. 10, pp. 9779–9793, Oct. 2019.

[3] P. Gao, Z. Tian, T. Pan, J. Wu, and W. Gui, "Transmission efficiency analysis and optimization of magnetically coupled resonant wireless power transfer system with misalignments," *AIP Adv.*, vol. 8, no. 8, Aug. 2018, Art. no. 085016.

[4] C. Zhang, D. Lin, and S. Y. Hui, "Basic control principles of omnidirectional wireless power transfer," *IEEE Trans. Power Electron.*, vol. 31, no. 7, pp. 5215–5227, Jul. 2016.

[5] Z. Zhang and B. Zhang, "Angular-misalignment insensitive omnidirectional wireless power transfer," *IEEE Trans. Ind. Electron.*, vol. 67, no. 4, pp. 2755–2764, Apr. 2020.

[6] J. Feng, Q. Li, F. C. Lee, and M. Fu, "Transmitter coils design for free-positioning omnidirectional wireless power transfer system," *IEEE Trans. Ind. Informat.*, vol. 15, no. 8, pp. 4656–4664, Aug. 2019.

[7] B. H. Choi, E. S. Lee, Y. H. Sohn, G. C. Jang, and C. T. Rim, "Six degrees of freedom mobile inductive power transfer by crossed dipole Tx and Rx coils," *IEEE Trans. Power Electron.*, vol. 31, no. 4, pp. 3252–3272, Apr. 2016.

[8] E. S. Lee, Y. H. Sohn, B. G. Choi, S. H. Han, and C. T. Rim, "A modularized IPt with magnetic shielding for a wide-range ubiquitous wi-power zone," *IEEE Trans. Power Electron.*, vol. 33, no. 11, pp. 9669–9690, Nov. 2018.

[9] B. G. Choi, Y.-H. Sohn, E. S. Lee, S. H. Han, H. R. Kim, and C. T. Rim, "Coreless transmitting coils with conductive magnetic shield for wide-range ubiquitous IPT," *IEEE Trans. Power Electron.*, vol. 34, no. 3, pp. 2539–2552, Mar. 2019.

[10] E. S. Lee, J. S. Choi, H. S. Son, S. H. Han, and C. T. Rim, "Six degrees of freedom wide-range ubiquitous IPT for IoT by DQ magnetic field," *IEEE Trans. Power Electron.*, vol. 32, no. 11, pp. 8258–8276, Nov. 2017.

[11] X. Yu, J. Feng, L. Zhu, and Q. Li, "Design and optimization of a planar omnidirectional wireless power transfer system for consumer electronics," *IEEE Open J. Power Electron.*, vol. 5, pp. 311–322, 2024.

[12] T. Feng, Y. Sun, Y. Feng, and X. Dai, "A tripolar plane-type transmitter for three-dimensional omnidirectional wireless power transfer," *IEEE Trans. Ind. Appl.*, vol. 58, no. 1, pp. 1254–1267, 2022.

[13] Y. Li, Y. Feng, and Y. Guo, "Free-positioning and omnidirectional wireless power transfer using self-decoupled planar transmitter coils," *IEEE Trans. Ind. Electron.*, vol. 71, no. 7, pp. 8091–8101, Jul. 2024.

[14] T. Feng, Z. Zuo, Y. Sun, X. Dai, X. Wu, and L. Zhu, "A reticulated planar transmitter using a three-dimensional rotating magnetic field for free-positioning omnidirectional wireless power transfer," *IEEE Trans. Power Electron.*, vol. 37, no. 8, pp. 9999–10015, Aug. 2022.

[15] T. Campi, S. Cruciani, F. Maradei, and M. Feliziani, "Magnetic field mitigation by multicoil active shielding in electric vehicles equipped with wireless power charging system," *IEEE Trans. Electromagn. Compat.*, vol. 62, no. 4, pp. 1398–1405, Aug. 2020.

[16] J. Kim et al., "Coil design and shielding methods for a magnetic resonant wireless power transfer system," *Proc. IEEE*, vol. 101, no. 6, pp. 1332–1342, Jun. 2013.

[17] H. Zhao et al., "Comprehensive investigation on the influence of magnetic materials on the weight and performance of onboard WPT systems," *IEEE Trans. Ind. Appl.*, vol. 58, no. 5, pp. 6842–6851, Sep./Oct. 2022.

[18] H.-R. Cha, K.-R. Park, T.-J. Kim, and R.-Y. Kim, "Design of magnetic structure for omnidirectional wireless power transfer," *IEEE Trans. Power Electron.*, vol. 36, no. 8, pp. 8849–8860, Aug. 2021.

Yi Li (Student Member, IEEE) was born in 1997. She received the B.Eng. degree in communication engineering from Soochow University, Suzhou, China, in 2019, and the M.Sc. degree in electrical engineering, in 2020, from the National University of Singapore, Singapore, where she is currently working toward the Ph.D. degree in electrical engineering with the Department of Electrical and Computer Engineering.

Her research interests include WPT technologies and power electronics.

Yuan Feng received the B.S. degree in automation from Southeast University, Nanjing, China, in 2014, and the Ph.D. degree in aeronautical and astronautical science and technology from Tsinghua University, Beijing, China, in 2020.

He is currently a Research Fellow with the National University of Singapore, Singapore. His research interests include neuromodulation technology, transcutaneous wireless communication technology, wireless power transmission for implants, implantable antenna and the application of electromagnetics and antenna technology in biomedical science and engineering.

Dr. Feng serves as a Reviewer for IEEE TRANSACTIONS ON ANTENNAS AND PROPAGATION, IEEE TRANSACTIONS ON BIOMEDICAL CIRCUITS AND SYSTEMS, *Frontiers in Physics*, and *Engineering*.

Yongxin Guo (Fellow, IEEE) received the B.Eng. and M.Eng. degrees in electronic engineering from the Nanjing University of Science and Technology, Nanjing, China, in 1992 and 1995, respectively, and the Ph.D. degree in electronic engineering from the City University of Hong Kong, Hong Kong, in 2001.

He is currently a Chair Professor of electronic engineering under the Global STEM Professorship Scheme with the Department of Electrical Engineering, City University of Hong Kong, Hong Kong. Concurrently, he is serving as Director for the City University of Hong Kong Qingdao Engineering Innovation Center, Hong Kong. He was a Professor with the Department of Electrical and Computer Engineering, National University of Singapore (NUS), Singapore. He has authored or coauthored more than 600 international journals and conference papers, two books, and four book chapters. He holds over 70 granted/filed patents in USA, China and Singapore. He has graduated 24 PhD students and hosted and supervised more than 110 research staff, visiting PhD students, and visiting scholars with NUS. His current research interests include electromagnetics in biomedicine, antennas, microwave, millimeter-wave and Terahertz Integrated Circuits, WPT, radar systems, microwaves in quantum computing, AI for antennas, RF circuits, and wireless sensing.

Dr. Guo was the recipient of 2020 IEEE Microwave and Wireless Components Letters Tatsuo Itoh Prize of the IEEE Microwave Theory and Techniques Society, and the CityU HK 1st EE Outstanding Alumni Award in 2022. He is a Fellow of the Singapore Academy of Engineering. He is serving as Editor-in-Chief for *IEEE Journal of Electromagnetics, RF and Microwaves in Medicine and Biology* for the term of 2020–2025. He is a Distinguished Lecturer for IEEE Antennas and Propagation Society (2022–2024). He is serving on the IEEE Biomedical Engineering Award Committee and on the IEEE Fellow Evaluation Committee for IEEE Engineering in Medicine and Biology Society (2019–2020). He was the Chair for IEEE AP-S Technical Committee on Antenna Measurement in 2018–2020. He served as Associate Editor for *IEEE Antennas and Wireless Propagation Letters* (2013–2018), *IET Microwaves, Antennas & Propagation* (2014–2017), *Electronics Letters* (2015–2019), *IEEE Journal of Electromagnetics, RF and Microwaves in Medicine and Biology* (2017–2020), and *IEEE Antennas and Propagation Magazine* (2018–2020). He has served as General Chair/Co-Chair for a number of international conferences/workshops.